ACS APPLIED MATERIALS & INTERFACES

www.acsami.org Research Article

Bicontinuous Nanoporous Nitrogen/Carbon-Codoped FeCoNiMg Alloy as a High-Performance Electrode for the Oxygen Evolution Reaction

Yuqian Huang, Feng Pei, Guang Ma, Zhiguo Ye,* Xinyuan Peng, Duosheng Li, and Zhong Jin*

Cite This: *ACS Appl. Mater. Interfaces* 2022, 14, 784−793 **Read Online**

ACCESS | Metrics & More | Article Recommendations | Supporting Information

Downloaded via NANJING UNIV on February 15, 2022 at 08:53:02 (UTC).
See https://pubs.acs.org/sharingguidelines for options on how to legitimately share published articles.

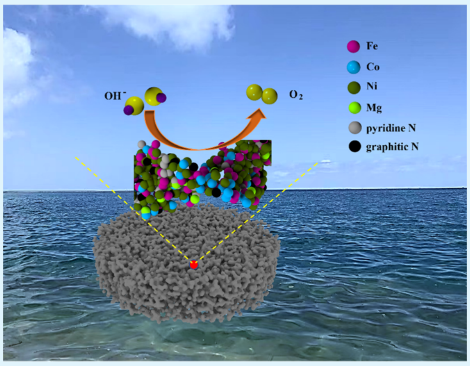

ABSTRACT: The kinetics of the oxygen evolution reaction (OER) in aqueous electrolytes is relatively slow, which seriously limits the energy efficiency of electricity-to-hydrogen conversion. Herein, a bicontinuous nanoporous FeCoNiMg alloy is prepared by high heat sintering method based on the nanoscale Kirkendall effect and the surface is codoped with nitrogen and carbon elements by the nitrocarburizing method (denoted NC-FeCoNiMg). The three-dimensional (3D) nanoporous NC-FeCoNiMg alloy electrode achieves superior electrocatalytic performance for the OER in alkaline media, delivering a low Tafel slope (34.6 mV dec^{-1}) and small overpotentials (235 and 290 mV at 10 and 100 mA cm^{-2}, respectively). Under consecutive high current densities, the NC-FeCoNiMg electrode still exhibits excellent long-term stability, and the OER activity even increases after testing for 100 h at a high current density of 1000 mA cm^{-2}. Comprehensive studies reveal that the N/C codoping of the inner and outer surfaces dramatically improves the electrocatalytic activity of the NC-FeCoNiMg electrode. This work demonstrates an efficient nanoarchitectural construction and a surface modulation strategy to increase the electrocatalytic activity and stability of transition-metal-based electrodes for the OER, holding great promise for fulfilling the requirements for the large-scale production of clean hydrogen energy.

KEYWORDS: *nanoporous alloy electrode, surface codoping, nitrocarburizing, oxygen evolution reaction, electrocatalytic activity and stability*

■ INTRODUCTION

Global environment and energy problems call for green and renewable energy sources as a substitute for fossil fuels.[1] As a secondary energy source, hydrogen energy has multiple advantages, such as cleanliness, nontoxicity, sustainability, high calorific value, and good combustion performance, making it an ideal alternative energy source.[2,3] Electrochemical water splitting is suitable for clean H_2 production, which can be split into the hydrogen evolution reaction (HER) of the cathode and oxygen evolution reaction (OER) of the anode. The OER is a four-electron oxidation process with slow kinetics.[4−6] Noble metal Ru/Ir and their composite materials exhibit remarkable merits of high electrocatalytic activity and long service life for the OER in aqueous media. However, the rare reserves and high costs of these precious metals hamper the large-scale application of electrochemical water electrolysis for clean H_2 production.[7−9] Therefore, it is imperative to develop inexpensive, easily synthesized OER electrocatalysts with an excellent electroactivity and long-term service performance.

A number of studies have been undertaken to explore various forms of transition-metal-based compounds (oxides,[10] (oxy)hydroxides,[11] sulfides,[12] selenides,[13] phosphides,[14,15] etc.), especially Ni, Co, and Fe-based materials, as OER electrocatalyst materials, exhibiting excellent electrochemical activities. A synergism due to the electronic structure reshaping of the active sites was discovered in multiple transition-metal-based compounds.[16−20] Hu and co-workers proved that the doping of Fe can alter the electronic structure of adjacent Ni and Co species to achieve a high OER electrocatalytic activity.[21] Wu et al. discovered that the incorporation of Ni/Fe-based electrode materials with Co can also increase the conductivity of electrocatalysts for the OER, improving the charge-transfer resistance and decreasing the overpotential.[22] Liu and co-workers successfully synthesized different metal (Fe, Co, and Ni) phosphide electrocatalysts supported on carbon nanofiber by a post-phosphorization method, which proved the synergistic effect for boosting the OER.[23] In

Received: September 28, 2021
Accepted: December 26, 2021
Published: January 4, 2022

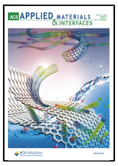

ACS Publications © 2022 American Chemical Society

https://doi.org/10.1021/acsami.1c18739

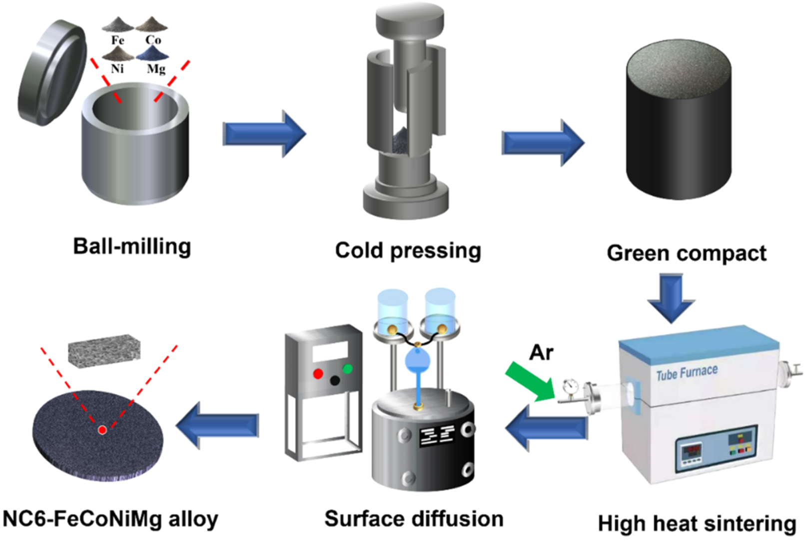

Figure 1. Schematic fabrication process for preparing the nanoporous NC6-FeCoNiMg alloy electrode.

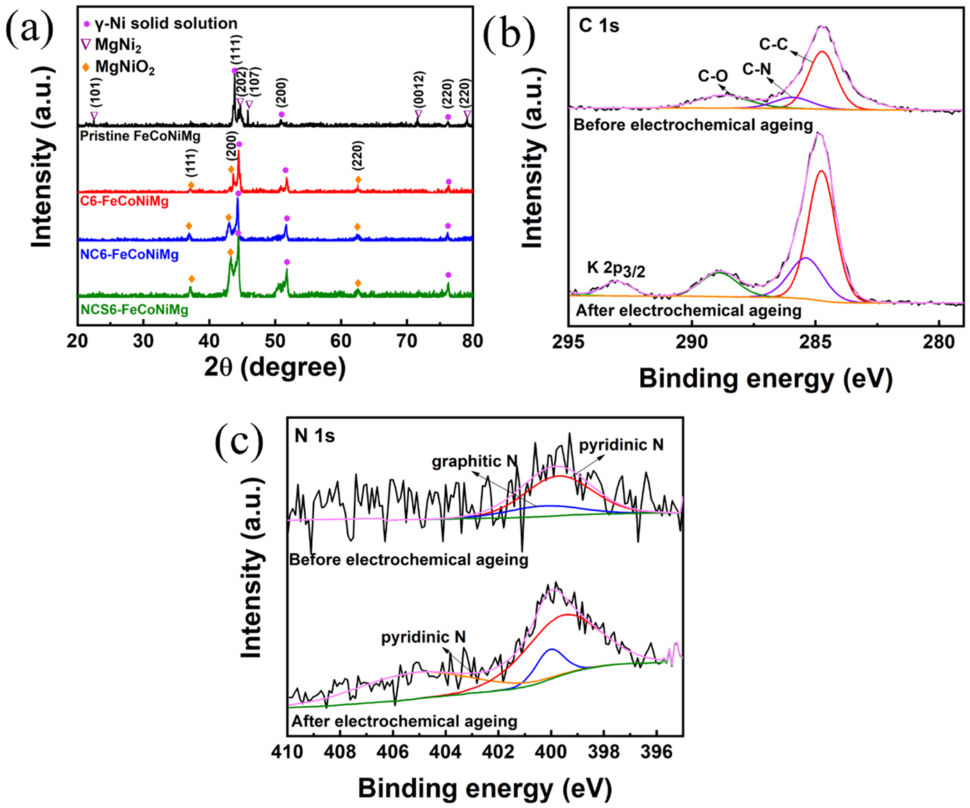

Figure 2. (a) XRD patterns of pristine FeCoNiMg, C6-FeCoNiMg, NC6-FeCoNiMg, and NCS6-FeCoNiMg. (b) C 1s and (c) N 1s XPS spectra of NC6-FeCoNiMg before and after electrochemical aging.

addition, various approaches were developed to adjust the compositions, morphologies, and properties of Ni−Fe−Co-based materials by coupling with various carbon materials, which can further improve the OER activity.[24−28] For example, doping carbon nanostructures with N heteroatoms can adjust the electronic structure of active sites and optimize the adsorption energies of key intermediates on the surface, which has been verified by many experiments and density functional theory (DFT) calculations for water splitting.[29−33] Zhou et al. applied the Fe leaching method to prepare a synergistic Ni−Fe alloy/NC composite, and the material exhibited a small overpotential of 290 mV at a current density of 20 mA cm^{-2} and Tafel slope of 76 mV dec^{-1} owing to the synergistic action of multiple species.[34]

In this work, we carried out preparation of a nanoporous alloy, nominally $Fe_{0.34}Co_{0.11}Ni_{0.55}$, by a high heat sintering method in an argon (Ar) atmosphere based on the nanoscale Kirkendall effect, as shown in Figure 1. Mg was used as the pore-making agent during the sintering process, and a small amount of Mg remained in the as-prepared alloy material. Nanoporous FeCoNiMg alloys (denoted FeCoNiMg) were further codiffused for 6 min with activated C, N/C, and N/C/

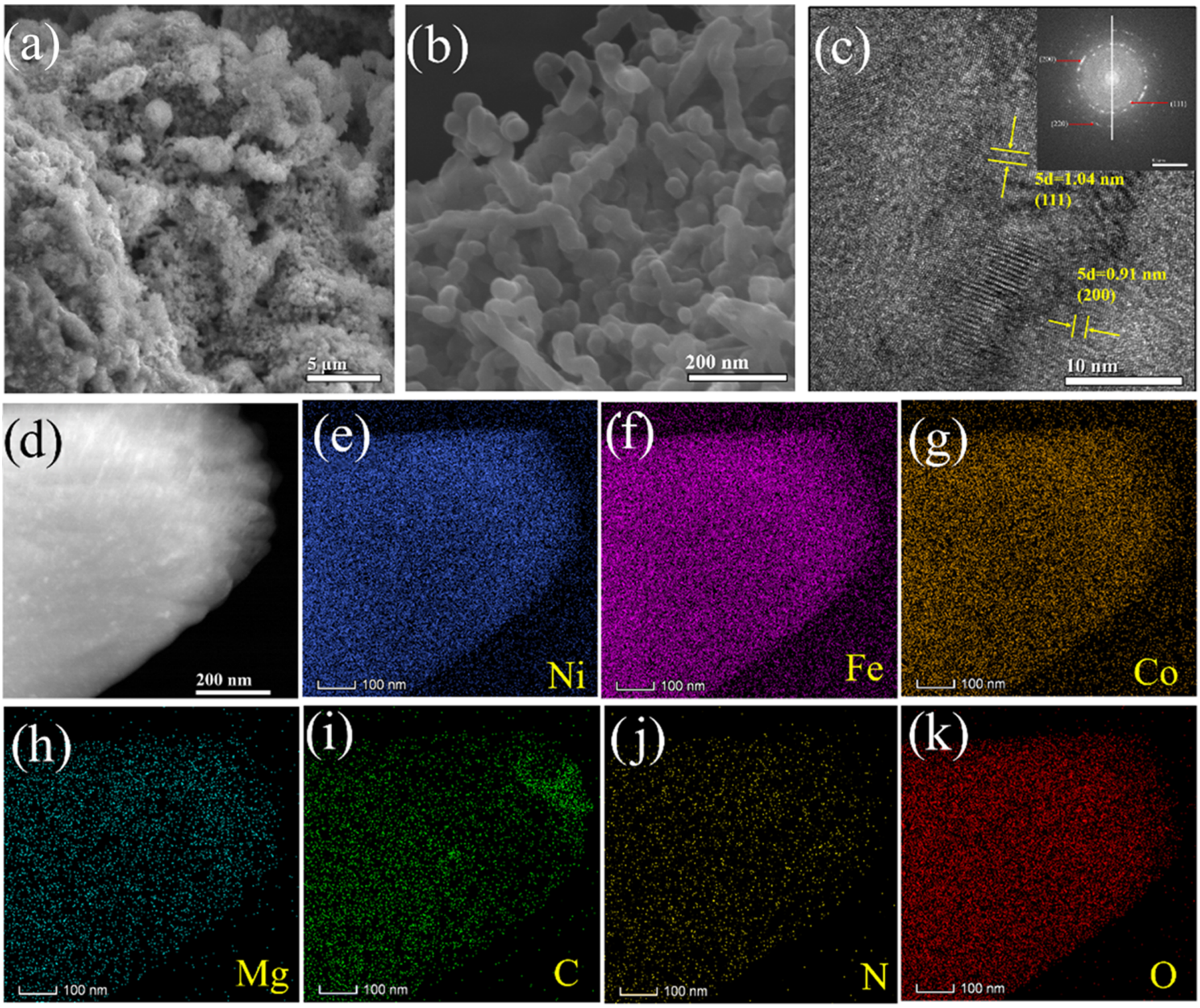

Figure 3. (a, b) FESEM images of nanoporous NC6-FeCoNiMg with different magnifications. (c) HRTEM and SAED patterns and (d) HAADF-STEM images of NC6-FeCoNiMg before electrochemical aging. EDX elemental mapping of (e) Ni, (f) Fe, (g) Co, (h) Mg, (i) C, (j) N, and (k) O in the unaged NC6-FeCoNiMg sample.

S species at the inner and outer surfaces via carburizing, nitrocarburizing, and sulfonitrocarburizing methods, respectively (denoted C6-FeCoNiMg, NC6-FeCoNiMg, and NCS6-FeCoNiMg, respectively). The as-prepared NC-FeCoNiMg alloy electrode exhibits superior electrocatalytic activity and excellent stability even at high current densities, and it holds great promise to serve as an advanced electrode material for the OER in alkaline media toward clean hydrogen production.

■ RESULTS AND DISCUSSION

Figure 1 shows the fabrication process of the nanoporous NC6-FeCoNiMg alloy. The nanoporous FeCoNiMg alloy is first fabricated by a high heat sintering method on account of the nanoscale Kirkendall effect in an Ar atmosphere and then the surface is codoped with N and C species via nitrocarburizing methods. The X-ray diffraction (XRD) curves of pristine FeCoNiMg, C6-FeCoNiMg, NC6-FeCoNiMg, and NCS6-FeCoNiMg samples are shown in Figure 2a. Clearly, the diffraction peaks of pristine FeCoNiMg located at 43.8, 50.0, and 75.0° correspond to the (111), (200), and (220) facets of a face-centered cubic (fcc) γ-Ni solid solution,[35] and the diffraction peaks located at 21.9, 44.8, 45.7, 71.7, and 79.4° correspond to the (101), (202), (107), (0012), and (220) facets of metallic $MgNi_2$ (JCPDS No. 25-1374). Hence, pristine FeCoNiMg should consist of a γ-Ni solid solution compound and some $MgNi_2$. As shown in Figure 2a, the diffraction peak intensities of C6-FeCoNiMg, NC6-FeCoNiMg, and NCS6-FeCoNiMg samples are obviously different from those of the pristine sample, which could be ascribed to the effects of C, N/C, and N/C/S diffusions at the inner and outer surfaces. Moreover, the XRD peaks located at 37.1, 43.1, and 62.6° correspond to the (111), (200), and (220) facets of metallic $MgNiO_2$ (JCPDS No. 24-0712), probably owing to the surface oxidation in the decomposed atmosphere during carburizing, nitrocarburizing, and sulfonitrocarburizing processes, as shown in Figures 2a and S1.

Figures 2b,c and S3 show the X-ray photoelectron spectroscopy (XPS) spectra of NC6-FeCoNiMg before and after electrochemical aging for 15 000 s at 10 mA cm^{-2} in a 1 M KOH solution. All of the XPS spectra are referenced to the

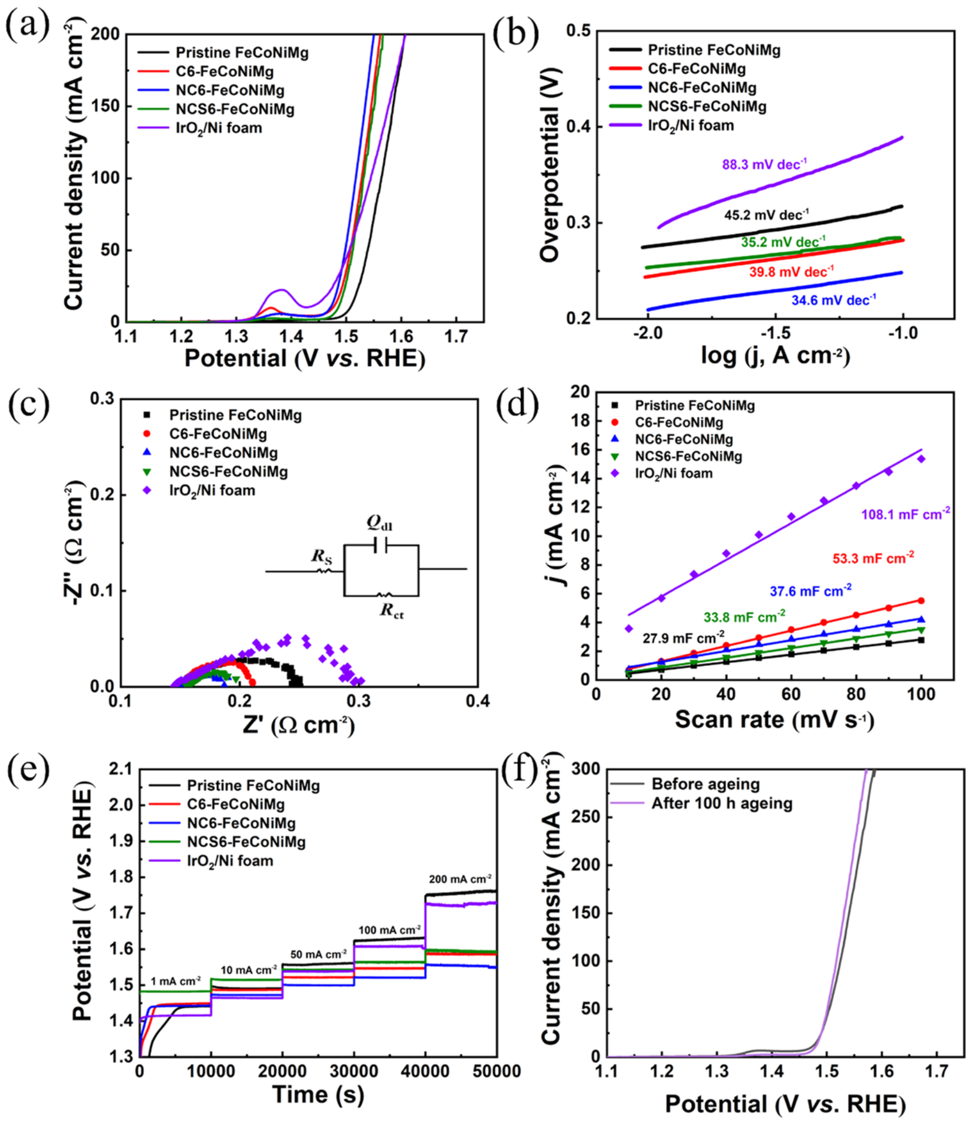

Figure 4. Electrochemical characterization of pristine FeCoNiMg, C6-FeCoNiMg, NC6-FeCoNiMg, NCS6-FeCoNiMg, and IrO_2/Ni foam electrodes in a 1 M KOH medium. (a) iR_s-uncorrected LSV plots of the electrodes measured with a scan rate of 1 mV s^{-1}. (b) Tafel plots of the electrodes originating from the data in panel (a). (c) Nyquist plots of the electrodes measured in a 1 M KOH medium. The equivalent circuit R_s ($Q_{dl}R_{ct}$) is inserted in the pattern. (d) C_{dl} values of the electrodes. (e) Galvanostatic tests of the electrodes obtained in a 1 M KOH medium at different current densities. (f) iR_s-uncorrected LSV curves of the NC6-FeCoNiMg electrode with a scan rate of 1 mV s^{-1} before and after electrochemical aging for 100 h at a current density of 1 A cm^{-2}.

main peak of C 1s at 284.8 eV. The XPS spectra in Figure S2 clearly confirm the presence of Co, Fe, Ni, Mg, N, C, and O species on the outermost surface of NC6-FeCoNiMg. As shown in Figure 2b, the C 1s spectrum can be divided into three peaks at 284.7, 285.9, and 288.7 eV, which are assigned to C−C, C−N, and C−O,[36] respectively. The peak at 293.1 eV corresponds to the K 2p band because the electrochemical aging process is performed in a KOH solution. Before electrochemical aging, the N 1s spectrum (Figure 2c) has two weak peaks at 398.2 eV (pyridinic N) and 400.6 eV (graphitic N).[34,37] Obviously, the profiles of the pyridinic N (398.7 and 405.2 eV) and graphitic N (400.8 eV) in the aged sample are more legible than those in the sample before electrochemical aging test, further confirming the surface diffusion of N species. Pyridinic N is apt to withdraw electrons, and graphitic N tends to donate electrons, both having an intrinsic impact on the electrocatalytic activity of the OER.[38,39] Moreover, the atomic ratio of N on the surface of the NC6-FeCoNiMg sample before and after electrochemical aging decreases from 0.46 to 0.30% (see Table S1), which should be ascribed to the dissolution of surface species during the process of OER. This consequence is also similar to the conclusion of the literature.[15] Two pairs of apparent peaks corresponding to Fe $2p_{3/2}$ (706.4 and 719.9 eV) and Fe $2p_{1/2}$ (710.2 and 724.1 eV) of metallic Fe[40] and Fe_2O_3[41] are observed in the unaged sample, as shown in Figure S3a. After electrochemical aging, the peaks of Fe $2p_{3/2}$ and Fe $2p_{1/2}$ located at 711.1 and 724.7 eV, respectively, are assigned to FeOOH,[42] indicating that surface structurization occurred during the initial stage of the OER. Similarly, Figure S3b shows Co 2p spectra. Before electrochemical aging, the two peaks of Co $2p_{3/2}$ at 780.2 eV and Co $2p_{1/2}$ at 795.4 eV and satellite peaks of Co $2p_{3/2}$ at 780.2 eV and Co $2p_{1/2}$ at 795.4 eV can be observed and are assigned to the Co−O bond of CoO.[43] After electrochemical aging, the Co 2p spectrum exhibits the expected doublets of Co $2p_{3/2}$ at 781.7 eV and Co $2p_{1/2}$ at 796.9 eV, which are assigned to the Co−OH bond of $Co(OH)_2$.[44] The Ni 2p spectrum of the unaged sample in Figure S3c shows two peaks of Ni $2p_{3/2}$ (853.9 and 871.3 eV) and Ni $2p_{1/2}$ (857.1 and 874.6 eV), which should correspond to Ni^{0+} and Ni_2O_3.[45] After electrochemical aging, Ni $2p_{3/2}$ and Ni $2p_{1/2}$ peaks located at 855.5 and 873.1 eV, respectively, can be attributed to Ni^{2+} signals derived from $Ni(OH)_2$.[46,47] In the Mg 2p spectrum of the unaged sample (Figure S3d), the peaks located at 49.5 and 50.8 eV correspond to metallic Mg (Mg^{0+}) and MgO. After electrochemical aging, the Mg 2p spectrum only exhibits one peak located at 49.5 eV, which corresponds to the phase of $Mg(OH)_2$.[48] Figure S3e shows that the O 1s spectrum was obtained before aging, in which the three peaks (529.4, 530.9, and 532.1 eV) correspond to M−O, M−OH, and adsorbed water molecules.[49,50] In contrast, the intensities of M−OH and M−O in the aged sample are higher and lower, respectively, than those in the unaged sample. It indicates that an (oxy)hydroxide layer composed of multiple species is formed on the surface of the aged sample during the OER process, which is consistent with the previous results.

Figure 3a,b shows the field emission scanning electron microscopy (FESEM) images of NC6-FeCoNiMg, revealing that the NC6-FeCoNiMg sample has bicontinuous nanopores and consists of interconnected nanoparticles, which gives rise to a BET surface area of 1.42 m^2 g^{-1}, an average pore diameter of 10.66 nm, and abundant active sites for the OER (see Figure S4 and Table S2). Figure 3c shows the high-resolution transmission electron microscopy (HRTEM) image of the unaged NC6-FeCoNiMg sample, which exhibits two interplanar spacings of 0.208 and 0.182 nm corresponding to the (111) and (200) crystal planes of the γ-Ni solid solution. The selected area diffraction pattern (SAED) further confirms the phase structure, which is also homologous with the XRD analysis of Figure 2a. Figure 3d−k presents the high-angle annular dark-field scanning TEM (HAADF-STEM) image and energy-dispersive X-ray (EDX) elemental mappings of the unaged NC6-FeCoNiMg sample. Clearly, Ni, Fe, Co, Mg, C, N, and O are uniformly distributed in this sample, further indicating the successful C and N codoping at the inner and outer surfaces by the nitrocarburizing method. Moreover, pristine FeCoNiMg and NC6-FeCoNiMg samples possess low water contact angles of 28.7 and 30.1°, respectively, exhibiting excellent wettability and hydrophilicity (see Figure S5). The dripping experiment further confirms the excellent wettability and hydrophilicity, which is favorable for increasing the electrocatalytic activity for the OER (see Videos S1 and S2).

Figure 4a shows linear sweep voltammetry (LSV) curves of pristine FeCoNiMg, C6-FeCoNiMg, NC6-FeCoNiMg, NCS6-FeCoNiMg, and IrO_2/Ni foam electrodes performed in a 1 M KOH medium with a scan rate of 1 mV s^{-1}. Compared to the IrO_2/Ni foam electrode, the nanoporous codoped FeCoNiMg alloy electrodes exhibit higher electrocatalytic activity; in particular, the NC6-FeCoNiMg electrode has the highest electrocatalytic activity of the OER. When the current density runs up to 10 mA cm^{-2}, pristine FeCoNiMg, C6-FeCoNiMg, NC6-FeCoNiMg, NCS6-FeCoNiMg, and IrO_2/Ni foam electrodes deliver different overpotentials of 259, 256, 235, 277, and 231 mV, respectively. When the OER current density reaches 100 mA cm^{-2}, pristine FeCoNiMg, C6-FeCoNiMg, NC6-FeCoNiMg, NCS6-FeCoNiMg, and IrO_2/Ni foam electrodes exhibit higher overpotentials of 378, 310, 290, 343, and 364 mV, respectively. A lower overpotential of 290 mV is achieved by the NC6-FeCoNiMg electrode at 100 mA cm^{-2}, indicating its superior electrocatalytic activity and fast kinetics for the OER. In addition, the NC6-FeCoNiMg electrode for the OER also exhibits the best electrocatalytic activity in all of the electrodes (see Figure S6 and Table S3). It was discovered that the electrocatalytic activity of the NC-FeCoNiMg alloy diffused by 6 min is higher than that of 3 and 10 min. Clearly, the nitrocarburizing time of 3 min cannot ensure an adequate codoped amount. However, the nitrocarburizing time of 10 min is easy to form carbon deposition that blocks the three-dimensional (3D) interconnected nanoporous structure, resulting in a rapid decrease of the electrocatalytic activity (see Figure S6). Undoubtedly, N and C codoping with a suited diffused time can greatly improve the OER activity of the NC6-FeCoNiMg electrode in a 1 M KOH medium. The main reason should be the formation of the pyridinic N and graphitic N on the alloy surface, improving the electron transfer and resulting in high conductivity for the electrode. It is also discovered that the FeCoNiMg alloy samples have a pre-OER oxidation peak in the potential range of 1.35−1.45 V (vs RHE), which is mainly derived from the surface oxidation of metals into a metal (oxy)hydroxide layer.[51−53]

To evaluate the oxygen evolution kinetics and reveal the OER mechanism, the Tafel slope and electrochemical impedance spectroscopy (EIS) data are measured as important indicators. Figure 4b shows that the iR_s-corrected Tafel slope (34.6 mV dec^{-1}) of the NC6-FeCoNiMg electrode is lower than those of pristine FeCoNiMg (45.2 mV dec^{-1}), C6-FeCoNiMg (39.8 mV dec^{-1}), NCS6-FeCoNiMg (35.2 mV dec^{-1}), and IrO_2/Ni foam (88.3 mV dec^{-1}) electrodes, further demonstrating the enhancement effect of N and C codoping induced by the nitrocarburizing process on the OER activity. The EIS data obtained from 0.01 to 100 kHz at a potential of 1.554 V (vs RHE) is analyzed using the equivalent circuit (R_s ($C_{dl}R_{ct}$)), as shown in Figure 4c, where R_s, C_{dl}, and R_{ct} denote the solution resistance, double-layer capacitance, and charge-transfer resistance during the OER process, respectively. Nyquist profiles exhibit a semicircle and provide the electron transfer rate that represents the OER kinetics of electrode materials. The NC6-FeCoNiMg electrode has a lowest R_{ct} value of ∼0.03 Ω cm^{-2} compared with those of pristine FeCoNiMg (0.16 Ω cm^{-2}), C6-FeCoNiMg (0.06 Ω cm^{-2}), NCS6-FeCoNiMg (0.04 Ω cm^{-2}), and IrO_2/Ni foam (0.18 Ω cm^{-2}) electrodes (see Table S4). This indicates the improvement in the electrocatalytic activity of the NC6-FeCoNiMg electrode owing to a decrease in the charge-transfer resistance caused by N and C codoping on the sample surface.[54] Moreover, the NC6-FeCoNiMg electrode can also achieve a high faradic efficiency of 98.9% in a 1 M KOH medium (see Figure S7).

The intrinsic activities of the as-prepared electrodes are further investigated. The specific activity of the electrocatalyst is the current per unit actual surface area at a given OER potential (i.e., mA cm^{-2}), mainly depending on the calculation of the electrochemical active surface area (ECSA). The ECSA is usually estimated using C_{dl} based on the cyclic voltammetry curve (CV) data. Figure 4d shows C_{dl} curves of pristine FeCoNiMg, C6-FeCoNiMg, NC6-FeCoNiMg, NCS6-FeCoNiMg, and IrO_2/Ni foam electrodes based on the data in Figure S8. The specific activity and ECSA can be estimated by eqs 1 and 2, respectively

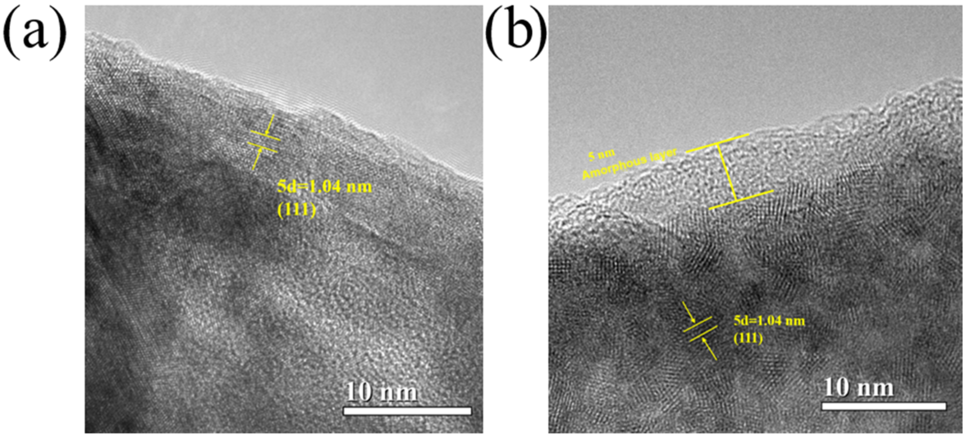

Figure 5. HRTEM images of the NC6-FeCoNiMg electrode (a) before and (b) after electrochemical aging for 300 cycles with a scan rate of 10 mV s^{-1} in the overpotential range of 1.054−1.604 V (vs RHE) in a 1 M KOH medium.

$$\text{specific activity} = \frac{I_{\mathrm{OER}}}{\mathrm{ECSA}} \tag{1}$$

$$\mathrm{ECSA} = \frac{C_{\mathrm{dl}}}{C^{\mathrm{s}}} \tag{2}$$

where I_{OER} is the OER current density at a given potential and C^{s} is the specific capacitance of the electrode material, which is usually assumed to be a universal value of 40 μF cm^{-2} for transition-metal oxide surfaces.[55] The C_{dl} values of pristine FeCoNiMg, C6-FeCoNiMg, NC6-FeCoNiMg, NCS6-FeCoNiMg, and IrO_2/Ni foam electrodes are 27.9, 53.3, 37.6, 33.8, and 108.1 mF cm^{-2}, respectively. Specific activities of all of the samples are calculated using OER current densities at a given potential of 1.6 V (vs RHE) in Figure 4a, as shown in Table S5. The NC6-FeCoNiMg electrode displays the highest specific activity (0.383 mA cm^{-2}) compared with those of pristine FeCoNiMg (0.262 mA cm^{-2}), C6-FeCoNiMg (0.243 mA cm^{-2}), NCS6-FeCoNiMg (0.334 mA cm^{-2}), and IrO_2/Ni foam (0.069 mA cm^{-2}) electrodes. This consequence should be ascribed to the N and C codoping on inner and outer surfaces of NC6-FeCoNiMg and the synergistic effects of multiple species.[56−60]

The long-term stability of electrocatalysts for the OER, especially at large current densities (≥1000 mA cm^{-2}), is another key indicator to evaluate the possibility of large-scale industrial applications. As shown in Figure 4e, the performances of pristine FeCoNiMg, C6-FeCoNiMg, NC6-FeCoNiMg, NCS6-FeCoNiMg, and IrO_2/Ni foam electrodes were measured during consecutive multicurrent steps from 1 to 200 mA cm^{-2} in a 1 M KOH medium for 50 000 s. When the current density of the OER runs up to 10 mA cm^{-2}, pristine FeCoNiMg, C6-FeCoNiMg, NC6-FeCoNiMg, NCS6-FeCoNiMg, and IrO_2/Ni foam electrodes achieve different overpotentials of 259, 256, 235, 277, and 231 mV, respectively. When the OER current density reaches 200 mA cm^{-2}, the NC6-FeCoNiMg electrode exhibits an overpotential of 330 mV, which is far lower than those of pristine FeCoNiMg (521 mV), C6-FeCoNiMg (358 mV), NCS6-FeCoNiMg (361 mV), and IrO_2/Ni foam (493 mV) electrodes, indicating its outstanding OER activity and excellent stability. The excellent OER performance and stability of the NC6-FeCoNiMg electrode are further confirmed by comparing with the previously reported electrocatalysts (see Table S6).

To further evaluate the OER stability, the electrode should be subjected to high current density operations for large-scale practical applications. A two-electrode cell is employed to assess the OER stability of the NC6-FeCoNiMg electrode at 1000 mA cm^{-2} for 100 h in a 1 M KOH medium (see Figure S9a). When performing the OER at 1000 mA cm^{-2} for the OER, the bath voltage of the NC6-FeCoNiMg electrode rapidly decreases and then remains ∼4.1 V over time (see Figure S9b), proving its excellent stability at large OER current densities. Figure 4f shows the LSV curves of the NC6-FeCoNiMg electrode before and after the OER for 100 h at 1000 mA cm^{-2}, obtained at a scan rate of 1 mV s^{-1} in a 1 M KOH aqueous medium. After the OER for 100 h, the OER activity of the NC6-FeCoNiMg electrode presents a small but clear increase, further indicating its excellent stability, which is ascribed to the high structural stability of the metal (oxy)hydroxide layer formed during the OER process. To verify this assumption, Figure 5a,b shows the HRTEM images of the NC6-FeCoNiMg electrode before and after electrochemical aging for 300 cycles in a 1 M KOH aqueous medium. As shown in Figure 5b, the surface structure of the NC6-FeCoNiMg electrode undergoes obvious rearrangement due to the formation of a metal (oxy)hydroxide layer of ∼5 nm thickness during the initial OER process, which is consistent with our previous results.[53] The (oxy)hydroxide layer in the inner and outer surfaces of the NC6-FeCoNiMg electrode also possesses more unsaturated active sites and defects compared to the pristine one, promoting the electron transfer of the OER.[61,62] All in all, long-term stability and excellent electrocatalytic activity of the nanoporous NC6-FeCoNiMg electrode are competitive with those of the reported electrocatalysts for the OER in an alkaline medium (see Table S6).

■ CONCLUSIONS

In summary, nanoporous FeCoNiMg alloys were successfully diffused with N, C, and S species on the inner and outer surfaces via facile and conventional carburizing, nitrocarburizing, and sulfonitrocarburizing methods, respectively. When serving as an electrode material for the OER, the nanoporous N/C-codoped FeCoNiMg alloy shows a low overpotential of 235 mV for 10 mA cm^{-2} and a small Tafel slope of 34.6 mV dec^{-1}. The NC6-FeCoNiMg electrode exhibits excellent stability without compromising on the electrocatalytic activity even at high current densities. The excellent OER activity and stability of the NC6-FeCoNiMg electrode can be ascribed to the high structural stability, large ECSA, excellent wettability, and N/C codoping on the inner and outer surfaces. This study provides a convenient strategy for the nanostructure construction and surface modulation of transition-metal alloy electrodes, which shows great potential for applications in the large-scale production of clean hydrogen energy.

EXPERIMENTAL SECTION

Electrode Preparation. Iron (12.7 μm, >99.5%), cobalt (13.7 μm, >99.5%), nickel (17.2 μm, >99.7%), and magnesium (75 μm, >99.9%) powders were bought from Aladdin Chemistry Corp. (Shanghai, China). Urea, methanol, $Na_2S_2O_3 \cdot 5H_2O$, and formamide were purchased from Xilong Scientific Industries, Co., Ltd. The IrO_2/Ni foam electrode as a control sample was prepared by the method of thermal decomposition described in our previous study.[53]

Preparation of the Nanoporous FeCoNiMg Alloy. Briefly, Co, Fe, and Ni powders were mixed in a mole ratio of 1:3:5, and spherical Mg powder (75 μm, 10 wt % total mass) was used as the pore-making agent. The preparation process of the nanoporous FeCoNiMg alloy is illustrated in Figure 1. First, a planetary ball mill (QM-3SP4, Nanjing University Instrument Plant) was employed to mix Fe, Co, Ni, and Mg powders at 250 rpm for 6 h. Then, the blended powders were cold-pressed to obtain green compacts in a mould (Φ 12 mm × 6 mm) under a uniaxial pressure of 580 MPa for 1 min. Afterward, the green compacts were placed in a tube furnace (OTF-1200X, Hefei Kejing Materials Technology Corp.) in an alumina crucible. Before sintering, highly pure argon (>99.999%) was added into the furnace tube for 20 min at a rate of 50 mL min^{-1} to eliminate the air. Finally, the FeCoNiMg alloy sample was sintered at 900 °C for 30 min and naturally cooled to room temperature in an Ar atmosphere.

Surface Diffusion. The as-prepared FeCoNiMg samples were cut into slices with a 1 mm thickness to dope the inner and outer surfaces with C, N/C, and N/C/S species via carburizing, nitrocarburizing, and sulfonitrocarburizing methods, respectively, as detailed below.

Carburizing. Liquid methanol was used as the carbon source and was dripped into the gas carburizing furnace with a power rating of 25 kW (RQ, Changxing Kaixiang Electric Furnace Technology Co., Ltd.) (see Figure S10) at ~4 mL min^{-1} and a temperature of 580 °C. The carburizing process times of C-FeCoNiMg were 3, 6, and 10 min (denoted C3-FeCoNiMg, C6-FeCoNiMg, and C10-FeCoNiMg, respectively). At 580 °C, liquid methanol in the gas carburizing furnace was decomposed according to the following reaction

$$2CH_3OH \rightarrow CO_2 + [C] + 4H_2 \qquad (3)$$

Thus, the decomposed [C] was diffused into the nanoporous FeCoNiMg alloy surface during the carburizing process.

Nitrocarburizing. Briefly, urea (56 g) was added to 500 mL of formamide, treated by gentle agitation at 50 °C for 30 min. The mixture was used as the source for N/C codoping by dripping into the gas carburizing furnace at ~4 mL min^{-1} and a temperature of 580 °C. The nitrocarburizing process times were 3, 6, and 10 min (denoted NC3-FeCoNiMg, NC6-FeCoNiMg, and NC10-FeCoNiMg, respectively). At 580 °C, the urea/formamide mixture in the gas carburizing furnace was decomposed according to the following reactions

$$4HCONH_2 \rightarrow 4[N] + 2[C] + 4H_2 + 2CO + 2H_2O \qquad (4)$$

$$2(NH_2)_2CO \rightarrow 4[N] + [C] + CO_2 + 4H_2 \qquad (5)$$

Thus, the decomposed [C] and [N] were diffused into the FeCoNiMg alloy surface during the nitrocarburizing process.

Sulfonitrocarburizing. $Na_2S_2O_3 \cdot 5H_2O$ (4.7 g) and urea (56 g) were added to 500 mL of formamide and treated by gentle agitation at 50 °C for 30 min. The mixture was used as the source for N/C/S codoping by dripping into the gas carburizing furnace at ~4 mL min^{-1} and a temperature of 580 °C. The sulfonitrocarburizing process times were 3, 6, and 10 min (denoted NCS3-FeCoNiMg, NCS6-FeCoNiMg, and NCS10-FeCoNiMg, respectively). At 580 °C, the mixture in the gas carburizing furnace was decomposed according to eqs 44−6

$$2Na_2S_2O_3 + 3O_2\ 2Na_2SO_4 + 2SO_2 \qquad (6)$$

Thus, the decomposed [C], [N], and [S] were diffused into the FeCoNiMg alloy surface during the sulfonitrocarburizing process.

Material Characterization Methods. The phases of the samples were identified by XRD (Bruker D8 ADVANCE) with Cu Kα as the radiation source. Surface morphologies, microstructures, and compositions of the samples were determined by FESEM (Nova Nano SEM 450), transmission electron microscopy (TEM, FEI Talos F200S A-TWIN), and energy-dispersive X-ray spectroscopy (EDS, Oxford Instruments). To identify the chemical compositions and electronic states, XPS (XPSINCA 250 X-max 50) was performed. The contact angles with Milli-Q water were measured by the sessile drop method using a KRUSS GmbH Germany (DO4010) goniometer; N_2 adsorption−desorption isotherms (Micromeritics ASAP 2460) were collected to measure the BET surface areas and average pore diameters.

Electrochemical Measurements. Electrochemical performances of the samples were evaluated on an electrochemical workstation (CHI-660C, Shanghai CHI Instruments, Inc.) using a standard three-electrode system in a 1.0 M KOH medium at 25 °C and ambient pressure. The as-prepared samples (1 cm^2), graphite rod, and saturated calomel electrode (SCE) were employed as the working, counter, and reference electrodes, respectively. A reversible hydrogen electrode (RHE) was used to calibrate the measured voltages (see Figure S11). LSV measurements were conducted with a scan rate of 1 mV s^{-1}. The Tafel slopes with an iR_s correction were achieved from the LSV curves, where R_s is the solution resistance obtained by EIS. The Nyquist plots were obtained by EIS with a 5 mV amplitude in the frequency range from 0.01 to 100 kHz. The ECSA was obtained by CV measurements of the capacitance of the C_{dl} at a non-faradic potential and different scan rates from 10 to 100 mV s^{-1}. The electrocatalytic stability of the as-prepared electrodes during the OER was performed at the OER current densities (i.e., 1, 10, 50, 100, and 200 mA cm^{-2}).

ASSOCIATED CONTENT

Supporting Information

The Supporting Information is available free of charge at https://pubs.acs.org/doi/10.1021/acsami.1c18739.

Wettability measurement of NC6-FeCoNiMg (MP4)

Wettability measurement of pristine FeCoNiMg (MP4)

XRD patterns of as-prepared nanoporous alloy electrodes; survey XPS spectra of the NC6-FeCoNiMg electrode before and after the OER test; water contact angle measurement of (a) pristine FeCoNiMg electrode and (b) NC6-FeCoNiMg electrode; LSV curves of the as-prepared electrodes in a 1 M KOH solution; photograph of gas carburizing furnace for carburizing, nitrocarburizing, and sulphonitrocarburizing processes; measured BET surface areas and average pore diameters of pristine FeCoNiMg, C6-FeCoNiMg, NC6-FeCoNiMg, and NCS6-FeCoNiMg electrodes; electrocatalytic performances of the electrodes at different overpotentials for the OER; and electrocatalytic performance comparison of electrodes for the OER (PDF)

AUTHOR INFORMATION

Corresponding Authors

Zhiguo Ye − *School of Materials Science and Engineering, Nanchang Hangkong University, Nanchang 330063, China;*
orcid.org/0000-0002-2669-8182;
Email: yezhiguo2008@163.com

Zhong Jin − *MOE Key Laboratory of Mesoscopic Chemistry, MOE Key Laboratory of High-Performance Polymer Materials and Technology, Jiangsu Key Laboratory of Advanced Organic Materials, Shenzhen Research Institute of Nanjing University, School of Chemistry and Chemical Engineering, Nanjing University, Nanjing 210023, China;* orcid.org/0000-0001-8860-8579; Email: zhongjin@nju.edu.cn

Authors

Yuqian Huang − *School of Materials Science and Engineering, Nanchang Hangkong University, Nanchang 330063, China*

Feng Pei − *State Grid JiangXi Electric Power Research Institute, Nanchang 330096, China*

Guang Ma − *Global Energy Interconnection Research Institute Co., Ltd., Beijing 102209, China*

Xinyuan Peng − *School of Materials Science and Engineering, Nanchang Hangkong University, Nanchang 330063, China*

Duosheng Li − *School of Materials Science and Engineering, Nanchang Hangkong University, Nanchang 330063, China*

Complete contact information is available at: https://pubs.acs.org/10.1021/acsami.1c18739

Notes

The authors declare no competing financial interest.

ACKNOWLEDGMENTS

This work was supported by the National Key Research and Development Program of China (2017YFA0208200), the Fundamental Research Funds for the Central Universities of China (0205-14380266), the National Natural Science Foundation of China (51862026, 51562027, 22022505, and 21872069), the Aeronautical Science Foundation of China (2017ZF56027), the Natural Science Foundation of Jiangxi Province (20192ACBL21048), the Key Research and Development Program of Jiangxi Province (20203BBE53069), the Natural Science Foundation of Jiangsu Province (BK20180008), and the Shenzhen Fundamental Research Program of Science, Technology and Innovation Commission of Shenzhen Municipality (JCYJ20180307155007589).

REFERENCES

(1) Chow, J.; Kopp, R. J.; Portney, P. R. Energy Resources and Global Development. *Science* **2003**, *302*, 1528−1531.

(2) Gao, M. Y.; Zeng, J. R.; Zhang, Q. B.; Yang, C.; Li, X. T.; Hua, Y. X.; Xu, C. Y. Scalable One-Step Electrochemical Deposition of Nanoporous Amorphous S Doped NiFe2O4/Ni3Fe Composite Films as Highly Efficient Electrocatalysts for Oxygen Evolution with Ultrahigh Stability. *J. Mater. Chem. A* **2018**, *6*, 1551−1560.

(3) Anantharaj, S.; Ede, S. R.; Sakthikumar, K.; Karthick, K.; Mishra, S.; Kundu, S. Recent Trends and Perspectives in Electrochemical Water Splitting with an Emphasis on Sulfide, Selenide, and Phosphide Catalysts of Fe, Co, and Ni: A Review. *ACS Catal.* **2016**, *6*, 8069−8097.

(4) Ye, M.-Y.; Li, S.; Zhao, X.; Tarakina, N. V.; Teutloff, C.; Chow, W. Y.; Bittl, R.; Thomas, A. Cobalt-Exchanged Poly(Heptazine Imides) as Transition Metal−Nx Electrocatalysts for the Oxygen Evolution Reaction. *Adv. Mater.* **2020**, *32*, No. 1903942.

(5) McCrory, C. C. L.; Jung, S.; Peters, J. C.; Jaramillo, T. F. Benchmarking Heterogeneous Electrocatalysts for the Oxygen Evolution Reaction. *J. Am. Chem. Soc.* **2013**, *135*, 16977−16987.

(6) Zhao, X.; Pachfule, P.; Li, S.; Simke, J. R. J.; Schmidt, J.; Thomas, A. Bifunctional Electrocatalysts for Overall Water Splitting from an Iron/Nickel-Based Bimetallic Metal−Organic Framework/Dicyandiamide Composite. *Angew. Chem., Int. Ed.* **2018**, *57*, 8921−8926.

(7) Ding, M.; Chen, J.; Jiang, M.; Zhang, X.; Wang, G. Ultrathin Trimetallic Metal-Organic Framework Nanosheets for Highly Efficient Oxygen Evolution Reaction. *J. Mater. Chem. A* **2019**, *7*, 14163−14168.

(8) Liu, G.; Yao, R.; Zhao, Y.; Wang, M.; Li, N.; Li, Y.; Bo, X.; Li, J.; Zhao, C. Encapsulation of Ni/Fe3O4 Heterostructures inside Onion-like N-Doped Carbon Nanorods Enables Synergistic Electrocatalysis for Water Oxidation. *Nanoscale* **2018**, *10*, 3997−4003.

(9) Kuang, M.; Zheng, G. Nanostructured Bifunctional Redox Electrocatalysts. *Small* **2016**, *12*, 5656−5675.

(10) Chen, Q.; Wang, R.; Lu, F.; Kuang, X.; Tong, Y.; Lu, X. Boosting the Oxygen Evolution Reaction Activity of NiFe2O4 Nanosheets by Phosphate Ion Functionalization. *ACS Omega* **2019**, *4*, 3493−3499.

(11) Zhang, Q.; Bedford, N. M.; Pan, J.; Lu, X.; Amal, R. A Fully Reversible Water Electrolyzer Cell Made Up from FeCoNi (Oxy)-Hydroxide Atomic Layers. *Adv. Energy Mater.* **2019**, *9*, No. 1901312.

(12) Chen, W.; Wang, H.; Li, Y.; Liu, Y.; Sun, J.; Lee, S.; Lee, J. S.; Cui, Y. In Situ Electrochemical Oxidation Tuning of Transition Metal Disulfides to Oxides for Enhanced Water Oxidation. *ACS Cent. Sci.* **2015**, *1*, 244−251.

(13) Zou, Z.; Wang, X.; Huang, J.; Wu, Z.; Gao, F. An Fe-Doped Nickel Selenide Nanorod/Nanosheet Hierarchical Array for Efficient Overall Water Splitting. *J. Mater. Chem. A* **2019**, *7*, 2233−2241.

(14) Xu, J.; Liu, Y.; Li, J.; Amorim, I.; Zhang, B.; Xiong, D.; Zhang, N.; Thalluri, S. M.; Sousa, J. P. S.; Liu, L. Hollow Cobalt Phosphide Octahedral Pre-Catalysts with Exceptionally High Intrinsic Catalytic Activity for Electro-Oxidation of Water and Methanol. *J. Mater. Chem. A* **2018**, *6*, 20646−20652.

(15) Li, W.; Xiong, D.; Gao, X.; Liu, L. The Oxygen Evolution Reaction Enabled by Transition Metal Phosphide and Chalcogenide Pre-Catalysts with Dynamic Changes. *Chem. Commun.* **2019**, *55*, 8744−8763.

(16) Shang, P.; Ye, Z.; Ding, Y.; Zhu, Z.; Peng, X.; Ma, G.; Li, D. Nanosponge-like Solid Solution of NiMo with a High Hydrogen Evolution Reaction Performance over a Wide Range of Current Densities. *ACS Sustainable Chem. Eng.* **2020**, *8*, 10664−10672.

(17) Cobo, S.; Heidkamp, J.; Jacques, P. A.; Fize, J.; Fourmond, V.; Guetaz, L.; Jousselme, B.; Ivanova, V.; Dau, H.; Palacin, S.; Fontecave, M.; Artero, V. A Janus Cobalt-Based Catalytic Material for Electro-Splitting of Water. *Nat. Mater.* **2012**, *11*, 802−807.

(18) Han, L.; Dong, S.; Wang, E. Transition-Metal (Co, Ni, and Fe)-Based Electrocatalysts for the Water Oxidation Reaction. *Adv. Mater.* **2016**, *28*, 9266−9291.

(19) Asnavandi, M.; Yin, Y.; Li, Y.; Sun, C.; Zhao, C. Promoting Oxygen Evolution Reactions through Introduction of Oxygen Vacancies to Benchmark NiFe-OOH Catalysts. *ACS Energy Lett.* **2018**, *3*, 1515−1520.

(20) Khalid, M.; Honorato, A. M. B.; Filho, G. T.; Varela, H. Trifunctional Catalytic Activities of Trimetallic FeCoNi Alloy Nanoparticles Embedded in a Carbon Shell for Efficient Overall Water Splitting. *J. Mater. Chem. A* **2020**, *8*, 9021−9031.

(21) Lee, S.; Banjac, K.; Lingenfelder, M.; Hu, X. Oxygen Isotope Labeling Experiments Reveal Different Reaction Sites for the Oxygen Evolution Reaction on Nickel and Nickel Iron Oxides. *Angew. Chem.* **2019**, *131*, 10401−10405.

(22) Wu, Z.; Wang, X.; Huang, J.; Gao, F. A Co-Doped Ni-Fe Mixed Oxide Mesoporous Nanosheet Array with Low Overpotential and High Stability towards Overall Water Splitting. *J. Mater. Chem. A* **2018**, *6*, 167−178.

(23) Xu, J.; Li, J.; Xiong, D.; Zhang, B.; Liu, Y.; Wu, K. H.; Amorim, I.; Li, W.; Liu, L. Trends in Activity for the Oxygen Evolution Reaction on Transition Metal (M = Fe, Co, Ni) Phosphide Pre-Catalysts. *Chem. Sci.* **2018**, *9*, 3470−3476.

(24) Hong, W.; Kitta, M.; Xu, Q. Bimetallic MOF-Derived FeCo-P/C Nanocomposites as Efficient Catalysts for Oxygen Evolution Reaction. *Small Methods* **2018**, *2*, No. 1800214.

(25) Li, Y.; Li, F. M.; Meng, X. Y.; Wu, X. R.; Li, S. N.; Chen, Y. Direct Chemical Synthesis of Ultrathin Holey Iron Doped Cobalt

Oxide Nanosheets on Nickel Foam for Oxygen Evolution Reaction. *Nano Energy* **2018**, *54*, 238−250.

(26) Zhuang, L.; Ge, L.; Liu, H.; Jiang, Z.; Jia, Y.; Li, Z.; Yang, D.; Hocking, R. K.; Li, M.; Zhang, L.; Wang, X.; Yao, X.; Zhu, Z. A Surfactant-Free and Scalable General Strategy for Synthesizing Ultrathin Two-Dimensional Metal−Organic Framework Nanosheets for the Oxygen Evolution Reaction. *Angew. Chem., Int. Ed.* **2019**, *58*, 13565−13572.

(27) Favaro, M.; Drisdell, W. S.; Marcus, M. A.; Gregoire, J. M.; Crumlin, E. J.; Haber, J. A.; Yano, J. An Operando Investigation of (Ni-Fe-Co-Ce)Ox System as Highly Efficient Electrocatalyst for Oxygen Evolution Reaction. *ACS Catal.* **2017**, *7*, 1248−1258.

(28) Le Formal, F.; Guijarro, N.; Bourée, W. S.; Gopakumar, A.; Prévot, M. S.; Daubry, A.; Lombardo, L.; Sornay, C.; Voit, J.; Magrez, A.; Dyson, P. J.; Sivula, K. A Gibeon Meteorite Yields a High-Performance Water Oxidation Electrocatalyst. *Energy Environ. Sci.* **2016**, *9*, 3448−3455.

(29) Deng, J.; Ren, P.; Deng, D.; Bao, X. Enhanced Electron Penetration through an Ultrathin Graphene Layer for Highly Efficient Catalysis of the Hydrogen Evolution Reaction. *Angew. Chem.* **2015**, *127*, 2128−2132.

(30) Fan, X.; Zhou, H.; Guo, X. WC Nanocrystals Grown on Vertically Aligned Carbon Nanotubes: An Efficient and Stable Electrocatalyst for Hydrogen Evolution Reaction. *ACS Nano* **2015**, *9*, 5125−5134.

(31) Wang, S.; Wang, J.; Zhu, M.; Bao, X.; Xiao, B.; Su, D.; Li, H.; Wang, Y. Molybdenum-Carbide-Modified Nitrogen-Doped Carbon Vesicle Encapsulating Nickel Nanoparticles: A Highly Efficient, Low-Cost Catalyst for Hydrogen Evolution Reaction. *J. Am. Chem. Soc.* **2015**, *137*, 15753−15759.

(32) Zhang, H.; Ma, Z.; Duan, J.; Liu, H.; Liu, G.; Wang, T.; Chang, K.; Li, M.; Shi, L.; Meng, X.; Wu, K.; Ye, J. Active Sites Implanted Carbon Cages in Core-Shell Architecture: Highly Active and Durable Electrocatalyst for Hydrogen Evolution Reaction. *ACS Nano* **2016**, *10*, 684−694.

(33) Li, Q.; Pan, H.; Higgins, D.; Cao, R.; Zhang, G.; Lv, H.; Wu, K.; Cho, J.; Wu, G. Metal-Organic Framework-Derived Bamboo-like Nitrogen-Doped Graphene Tubes as an Active Matrix for Hybrid Oxygen-Reduction Electrocatalysts. *Small* **2015**, *11*, 1443−1452.

(34) Zhou, Y.; Li, Y.; Zhang, L.; Zhang, L.; Li, L.; Tian, J.; Wang, M.; Xu, J.; Dai, B.; Li, Y. Fe-Leaching Induced Surface Reconstruction of Ni-Fe Alloy on N-Doped Carbon to Boost Oxygen Evolution Reaction. *Chem. Eng. J.* **2020**, *394*, No. 124977.

(35) Villars, P.; Calvert, L. D. *Pearson's Handbook of Crystallographic Data for Intermetallic Phases*, 2nd ed.; ASM: Metals Park, Ohio, 1991; pp 4−6.

(36) Zhang, X.; Li, C.; Si, T.; Lei, H.; Wei, C.; Sun, Y.; Zhan, T.; Liu, Q.; Guo, J. FeNi Cubic Cage@N-Doped Carbon Coupled with N-Doped Graphene toward Efficient Electrochemical Water Oxidation. *ACS Sustainable Chem. Eng.* **2018**, *6*, 8266−8273.

(37) Lei, C.; Chen, H.; Cao, J.; Yang, J.; Qiu, M.; Xia, Y.; Yuan, C.; Yang, B.; Li, Z.; Zhang, X.; Lei, L.; Abbott, J.; Zhong, Y.; Xia, X.; Wu, G.; He, Q.; Hou, Y. Fe N 4 Sites Embedded into Carbon Nanofiber Integrated with Electrochemically Exfoliated Graphene for Oxygen Evolution in Acidic Medium. *Adv. Energy Mater.* **2018**, *8*, No. 1801912.

(38) Yang, H. B.; Miao, J.; Hung, S.-F.; Chen, J.; Tao, H.-B.; Wang, X.; Zhang, L.; Chen, R.; Gao, J.; Chen, H. M.; Dai, L.; Liu, B. Identification of Catalytic Sites for Oxygen Reduction and Oxygen Evolution in N-Doped Graphene Materials: Development of Highly Efficient Metal-Free Bifunctional Electrocatalyst. *Sci. Adv.* **2016**, *2*, No. e1501122.

(39) Liu, Z.; Yu, X.; Yu, H.; Xue, H.; Feng, L. Nanostructured FeNi3 Incorporated with Carbon Doped with Multiple Nonmetal Elements for the Oxygen Evolution Reaction. *ChemSusChem* **2018**, *11*, 2703−2709.

(40) Liu, Z.; Tang, B.; Gu, X.; Liu, H.; Feng, L. Selective Structure Transformation for NiFe/NiFe2O4 Embedded Porous Nitrogen-Doped Carbon Nanosphere with Improved Oxygen Evolution Reaction Activity. *Chem. Eng. J.* **2020**, *395*, No. 125170.

(41) Nsanzimana, J. M. V.; Reddu, V.; Peng, Y.; Huang, Z.; Wang, C.; Wang, X. Ultrathin Amorphous Iron−Nickel Boride Nanosheets for Highly Efficient Electrocatalytic Oxygen Production. *Chem. - Eur. J.* **2018**, *24*, 18502−18511.

(42) Feng, J. X.; Ye, S. H.; Xu, H.; Tong, Y. X.; Li, G. R. Design and Synthesis of FeOOH/CeO2Heterolayered Nanotube Electrocatalysts for the Oxygen Evolution Reaction. *Adv. Mater.* **2016**, *28*, 4698−4703.

(43) Kuang, X.; Kang, B.; Wang, Z.; Gao, L.; Guo, C.; Lee, J. Y.; Sun, X.; Wei, Q. Sulfur-Doped CoO Nanoflakes with Loosely Packed Structure Realizing Enhanced Oxygen Evolution Reaction. *Chem. - Eur. J.* **2018**, *24*, 17288−17292.

(44) Pei, L.; Ye, Z.; Yuan, X.; Peng, X.; Li, D.; Zheng, Z. Three-Dimensional CoMoMg Nanomesh Based on the Nanoscale Kirkendall Effect for the Efficient Hydrogen Evolution Reaction. *J. Alloys Compd.* **2021**, *857*, No. 158086.

(45) Huang, Y.; Hu, L.; Liu, R.; Hu, Y.; Xiong, T.; Qiu, W.; Balogun, M. S. J. T.; Pan, A.; Tong, Y. Nitrogen Treatment Generates Tunable Nanohybridization of Ni5P4 Nanosheets with Nickel Hydr(Oxy)-Oxides for Efficient Hydrogen Production in Alkaline, Seawater and Acidic Media. *Appl. Catal., B* **2019**, *251*, 181−194.

(46) Biesinger, M. C.; Payne, B. P.; Lau, L. W. M.; Gerson, A.; Smart, R. S. C. X-Ray Photoelectron Spectroscopic Chemical State Quantification of Mixed Nickel Metal, Oxide and Hydroxide Systems. *Surf. Interface Anal.* **2009**, *41*, 324−332.

(47) Zhang, J.; Yu, L.; Chen, Y.; Lu, X. F.; Gao, S.; Lou, X. W. Designed Formation of Double-Shelled Ni−Fe Layered-Double-Hydroxide Nanocages for Efficient Oxygen Evolution Reaction. *Adv. Mater.* **2020**, *32*, No. 1906432.

(48) Luo, Y.; Sun, Y.; Lv, J.; Wang, X.; Li, J.; Wang, F. Transition of Interface Oxide Layer from Porous Mg(OH)2 to Dense MgO Induced by Polyaniline and Corrosion Resistance of Mg Alloy Therefrom. *Appl. Surf. Sci.* **2015**, *328*, 247−254.

(49) Xie, C.; Wang, Y.; Hu, K.; Tao, L.; Huang, X.; Huo, J.; Wang, S. In Situ Confined Synthesis of Molybdenum Oxide Decorated Nickel-Iron Alloy Nanosheets from MoO42- Intercalated Layered Double Hydroxides for the Oxygen Evolution Reaction. *J. Mater. Chem. A* **2017**, *5*, 87−91.

(50) Masa, J.; Sinev, I.; Mistry, H.; Ventosa, E.; de la Mata, M.; Arbiol, J.; Muhler, M.; Roldan Cuenya, B.; Schuhmann, W. Ultrathin High Surface Area Nickel Boride (NixB) Nanosheets as Highly Efficient Electrocatalyst for Oxygen Evolution. *Adv. Energy Mater.* **2017**, *7*, No. 1700381.

(51) Xu, K.; Chen, P.; Li, X.; Tong, Y.; Ding, H.; Wu, X.; Chu, W.; Peng, Z.; Wu, C.; Xie, Y. Metallic Nickel Nitride Nanosheets Realizing Enhanced Electrochemical Water Oxidation. *J. Am. Chem. Soc.* **2015**, *137*, 4119−4125.

(52) Louie, M. W.; Bell, A. T. An Investigation of Thin-Film Ni-Fe Oxide Catalysts for the Electrochemical Evolution of Oxygen. *J. Am. Chem. Soc.* **2013**, *135*, 12329−12337.

(53) Hao, B.; Ye, Z.; Xu, J.; Li, L.; Huang, J.; Peng, X.; Li, D.; Jin, Z.; Ma, G. A High-Performance Oxygen Evolution Electrode of Nanoporous Ni-Based Solid Solution by Simulating Natural Meteorites. *Chem. Eng. J.* **2021**, *410*, No. 128340.

(54) Wang, Z.; Lu, Y.; Yan, Y.; Larissa, T. Y. P.; Zhang, X.; Wuu, D.; Zhang, H.; Yang, Y.; Wang, X. Core-Shell Carbon Materials Derived from Metal-Organic Frameworks as an Efficient Oxygen Bifunctional Electrocatalyst. *Nano Energy* **2016**, *30*, 368−378.

(55) Wei, C.; Sun, S.; Mandler, D.; Wang, X.; Qiao, S. Z.; Xu, Z. J. Approaches for Measuring the Surface Areas of Metal Oxide Electrocatalysts for Determining Their Intrinsic Electrocatalytic Activity. *Chem. Soc. Rev.* **2019**, *48*, 2518−2534.

(56) Friebel, D.; Louie, M. W.; Bajdich, M.; Sanwald, K. E.; Cai, Y.; Wise, A. M.; Cheng, M. J.; Sokaras, D.; Weng, T. C.; Alonso-Mori, R.; Davis, R. C.; Bargar, J. R.; Nørskov, J. K.; Nilsson, A.; Bell, A. T. Identification of Highly Active Fe Sites in (Ni,Fe)OOH for

Electrocatalytic Water Splitting. *J. Am. Chem. Soc.* **2015**, *137*, 1305−1313.

(57) Stevens, M. B.; Enman, L. J.; Korkus, E. H.; Zaffran, J.; Trang, C. D. M.; Asbury, J.; Kast, M. G.; Toroker, M. C.; Boettcher, S. W. Ternary Ni-Co-Fe Oxyhydroxide Oxygen Evolution Catalysts: Intrinsic Activity Trends, Electrical Conductivity, and Electronic Band Structure. *Nano Res.* **2019**, *12*, 2288−2295.

(58) Septiani, N. L. W.; Kaneti, Y. V.; Fathoni, K. B.; Kani, K.; Allah, A. E.; Yuliarto, B.; Nugraha; Dipojono, H. K.; Alothman, Z. A.; Golberg, D.; Yamauchi, Y. Self-Assembly of Two-Dimensional Bimetallic Nickel-Cobalt Phosphate Nanoplates into One-Dimensional Porous Chainlike Architecture for Efficient Oxygen Evolution Reaction. *Chem. Mater.* **2020**, *32*, 7005−7018.

(59) Zhang, X.; Zhang, L.; Zhu, Y.; Li, Z.; Wang, Y.; Wågberg, T.; Hu, G. Increasing Electrocatalytic Oxygen Evolution Efficiency through Cobalt-Induced Intrastructural Enhancement and Electronic Structure Modulation. *ChemSusChem* **2021**, *14*, 467−478.

(60) Pan, J.; Hao, S.; Zhang, X.; Huang, R. In Situ Growth of Fe and Nb Co-Doped β-Ni(OH)2nanosheet Arrays on Nickel Foam for an Efficient Oxygen Evolution Reaction. *Inorg. Chem. Front.* **2020**, *7*, 3465−3474.

(61) Jiang, B.; Wan, Z.; Kang, Y.; Guo, Y.; Henzie, J.; Na, J.; Li, H.; Wang, S.; Bando, Y.; Sakka, Y.; Yamauchi, Y. Auto-Programmed Synthesis of Metallic Aerogels: Core-Shell Cu@Fe@Ni Aerogels for Efficient Oxygen Evolution Reaction. *Nano Energy* **2021**, *81*, No. 105644.

(62) Huang, Z. F.; Song, J.; Du, Y.; Xi, S.; Dou, S.; Nsanzimana, J. M. V.; Wang, C.; Xu, Z. J.; Wang, X. Chemical and Structural Origin of Lattice Oxygen Oxidation in Co−Zn Oxyhydroxide Oxygen Evolution Electrocatalysts. *Nat. Energy* **2019**, *4*, 329−338.